CEAS-GNC-2022-020

CEAS EuroGNC 2022
"Conference on Guidance, Navigation and Control"
3-5 May 2022 @ Technische Universität Berlin, Germany

Definition of a Landing Strategy for a Model-Scale Reusable Rocket

Nicolas Bourliatoux Undergraduate Research Assistant, ISAE-SUPAERO, Université de Toulouse, France. nicolas.bourliatoux@student.isae-supaero.fr

Joan M. Riera Undergraduate Research Assistant, ISAE-SUPAERO, Université de Toulouse, France. joan.moya-riera@student.isae-supaero.fr

Leandro R. Lustosa Assistant Professor, ISAE-SUPAERO, Université de Toulouse, France. leandro.lustosa@isae-supaero.fr

ABSTRACT

Model-scale rockets differ from their real-size counterparts in important ways. For one, the lack of significant thrust throttling limits retro propulsion landing capabilities. This paper studies its feasibility by employing model-scale non-throttleable solid-propellant engines. Our landing strategy comprises an aerodynamic passive descent followed by a thrust vector control touchdown, and thus thrust is modulated not by magnitude but by direction. This strategy imposes additional levels of under-actuation and nonlinearities that cannot be easily tackled with linear approaches. We propose a Nonlinear Model Predictive Controller as a solution and test its performance and robustness in simulation in different scenarios.

Keywords: Model-Scale Rocket; Autonomous Landing; Thrust Vectoring; Nonlinear Model Predictive Control.

1 Introduction

In the recent past, almost every component of a rocket sent into orbit was designed to be used just once. The first rocket stage, spanning between 70 to 80 percent of the total cost, was destroyed in the atmosphere during reentry. The reusable rocket paradigm [1, 2] aims to reduce the number of resources lost. While still a relatively new technology, reusable rockets have multiple benefits, including time, capital, and material saving, which have turned space exploration into a more accessible and sustainable endeavor.

Landing and launching from Earth are particularly challenging due to the high levels of aerodynamic and thermal stress induced by its dense atmosphere on the vehicle's structure, which is further worsened by the existence of uncertain and time-varying wind perturbations. These effects become more adverse for the next generation of launchers, as they present lighter and more flexible structures, leading to stronger control-structure couplings.

As a rocket's size and weight decrease, its architectural complexity issues shift: scale models are assembled with single-use engines, cardboard bodies, and lightweight molded clay nozzles. Their flight domain differs too: altitude and speed values are lower with different aerodynamics. Thus, scale models don't suffer as much from aerothermal stresses. However, low inertia makes model-scale rockets highly unstable against applied forces and torques. Additionally, the reduced size of the vehicle restrains the

available computing power and allows only for solid-propellant — thus non-throttleable — motors. Accordingly, adapted versions of the control algorithms are necessary to stabilize the rocket in real-time.

This work focuses on model-scale rocketry and we carry out this project in collaboration with the Space Section student club of ISAE-SUPAERO with the ultimate goal of safely recovering flight data recorded onboard a model-scale rocket. We believe that model-scale vehicles are good candidates for benchmarking design techniques and, additionally, provide challenging control problems (we difer them from reduced-size demonstrators [3] that are designed for exploring specific hypotheses). As for their recovery, parachutes are commonplace but novel techniques are still being investigated [4]. At the same time, no program successfully achieved touchdown using solid-propellant retro propulsion to the best of the authors' knowledge. The main reason is the solid propellant motor often cuts out too early or too late while tracking a fixed open-loop trajectory. A compelling control problem is then evident: is it possible to robustly land a non-throttleable rocket?

To the best of the authors' knowledge, there is no previous scientific work on this particular question. This work explores the existence problem by providing a two-phase guidance strategy for autonomous landing similar to its throttleable counterpart in [5]. The first consists of an initial aerodynamic control phase defined in Sec. 2, leading the rocket from the apogee of the trajectory to a predefined altitude and speed where engine ignition takes place. This comprises aerodynamics studies similar to [6, 7]. Although we use passive control, previous work [8] uses Nonlinear Model Predictive Control (NMPC) to optimize and track trajectories.

The second phase is defined in Sec. 3, where the rocket is safely guided from the ignition point to the ground using NMPC. NMPC is commonplace in autonomous rocket landing research and its high computational cost is its main drawback. Therefore, a myriad of papers [9–12] investigate numerical tricks involving convexication of the problem or relaxation of constraints. Additionally, Ref. [13] studies NMPC in the context of an electric throttleable model-scale reusable rocket with successful experimental flights. Finally, Sec. 4 concludes with remarks for future work.

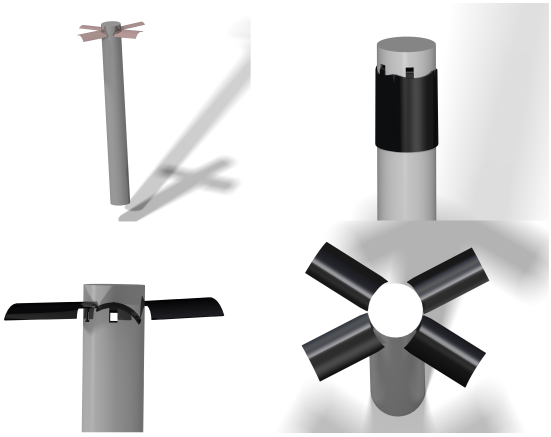

Fig. 1 Rocket and fins CAD model.

2 Aerodynamic Passive Descent Phase

We propose an alternative aerodynamic actuator to the commonplace grid fins, consisting of four quarters of a cylinder, deployable as shown in Fig. 1. By independently changing their opening angles, this system enables roll, pitch, and yaw control — similarly to grid fins — and stabilizes the rocket passively during its descent. Additionally, it adds velocity control while descending. This control over speed is vital for transitioning to the second landing phase using a model-scale solid-propellant engine with limited thrust.

2.1 System Description

The fins used for this study are designed to maximize drag at full deployment and minimize it when retracted. Therefore, they have little impact on the lift-off dynamics when closed and act as part of the rocket's external skin. At the apogee, the fins open at slight angles to create just enough drag to reduce acceleration at high altitudes while controlling its orientation and direction. By applying slightly different angles to the four fins, the symmetry of the aerodynamic forces on the rocket is broken, thus inducing controllable moments in roll, pitch, and yaw. As the rocket descends and reaches its terminal velocity, the fins will further open to slow it down as adaptable airbrakes.

The fins being radially asymmetrical, as shown in Fig. 1, they individually create orthoradial lift. Due to the fins' chosen symmetries around the rocket's central axis, this lift enables a decoupled control of roll, pitch, yaw, and velocity by coordinating the angles of the four fins.

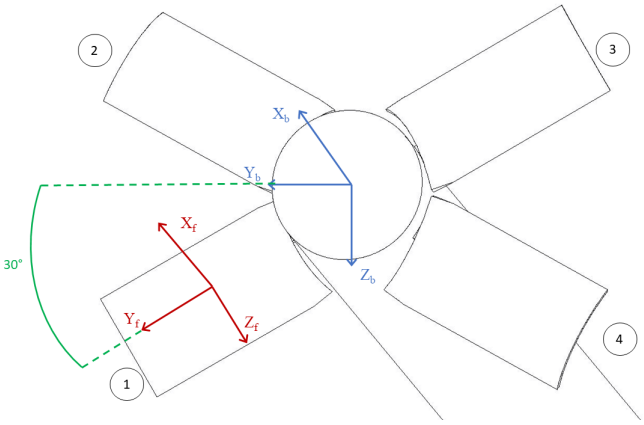

Fig. 2 Body and fin frames.

The model-scale rocket considered for the experiment measures 70 cm long with a fuselage diameter of 7.4 cm. The total mass is 3 kg with a center of inertia at 25% of the rocket's length, as the engine represents the large majority of the total mass. The fins measure 10 cm long and are 5.32 cm wide and are attached at $9/10$th of the rocket's height, each fin being a quarter of a cylinder of 7.6 cm diameter. The fins' links are rotated at an angle of 15° around the cylinder's axis with respect to the center of the fin.

As shown in Fig. 2, a fin frame is centered on the middle of each fin and with a rotation of 30° around the body frame X_b axis. This angle of 30° enables the fins to close into a full cylinder around the fuselage while having the individual asymmetry in the $X_\mathrm{f}Y_\mathrm{f}$ plane needed to induce lift along Z_f. The angle between the fin's Y_f axis and the fuselage of the rocket is hereafter referred to as κ, with κ_i holding the angle of the i-th fin, such that

$$\kappa = \pi - \boldsymbol{X}_\mathrm{b} \cdot \boldsymbol{Y}_\mathrm{f} \tag{1}$$

2.2 Aerodynamic Coefficients Identification

A 3D fins model was used to run computer fluid dynamics (CFD) simulations on `StarCCM+`. We set the simulation to assume air in a steady segregated flow, at constant density, and under k-omega turbulence. The meshing is rectangular with a base size of 5 mm and a re-meshing around the fin of 1.25 mm (25% of base size). Under these conditions, the simulation results yielded a terminal velocity with fully closed fins at around 80 $\mathrm{m\,s^{-1}}$.

Figure 3 shows the velocity profiles around the fin in the $X_\mathrm{f}Z_\mathrm{f}$ and $X_\mathrm{f}Y_\mathrm{f}$ planes for a fully deployed fin (Figs. 3a and 3b) and at an angle of 70° (Figs 3c and 3d). The asymmetric vortexes behind the fin create lift along the Z_f-axis, as needed, and along the Y_f-axis when the κ angle is less than 90°. The lift induced along the Y_f-axis is not considered for the aerodynamic model defined below, as the $\Delta\kappa$ angles in-between the fin angles are small compared to the κ angles.

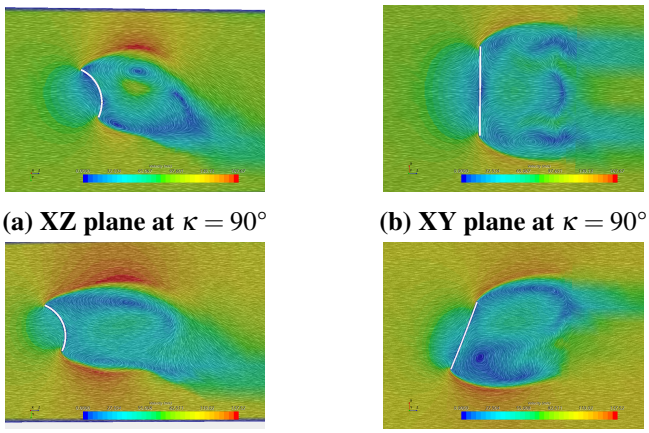

(a) XZ plane at $\kappa = 90°$ **(b) XY plane at $\kappa = 90°$**

(c) XZ plane at $\kappa = 70°$ **(d) XY plane at $\kappa = 70°$**

Fig. 3 Fin airflow for two planes and for two κ angle values.

The simulations run for several κ angles returned the evolution of the drag and lift coefficients C_xf and C_zf for a fin at 100 $\mathrm{m\,s^{-1}}$ as follows

- At $\kappa = \pi/2$,

$$\begin{cases} C_{\mathrm{xf}} = 1.55 \\ C_{\mathrm{zf}} = 1.28 \end{cases} \tag{2}$$

- For $\kappa < \pi/2$,

$$\begin{cases} C_{\mathrm{xf}} = 1.55 \sin\kappa \\ C_{\mathrm{zf}} = 1.28 \sin\kappa \end{cases} \tag{3}$$

To simplify the dynamics model, we only take into account the drag and lift coefficients of each fin and the drag coefficient of the bottom section of the fuselage. All moments' coefficients are neglected. Therefore, the forces applied to the rocket are its weight and drag only. Additionally, the resultant moments are the roll, pitch, and yaw torques induced by the unequal lever arms and drag forces applied on each fin when the κ_i angles are unequal.

2.3 Dynamics Model for Aerodynamic Passive Control

Employing the Euler angles formulation for attitude, the dynamics simulator was implemented on `Simulink`. The body frame $(X_{\mathrm{b}}, Y_{\mathrm{b}}, Z_{\mathrm{b}})$ is oriented such that X_{b} aligns with the symmetry axis of the rocket and is directed towards the nose cone. The system actuators are defined as

$$u = (\kappa_1, \kappa_2, \kappa_3, \kappa_4) \tag{4}$$

where κ_i is the angle between the fuselage and the Y_{f} axis of the i-th fin. The resulting system state is defined as

$$x = (X_{\mathrm{e}}, Y_{\mathrm{e}}, Z_{\mathrm{e}}, \phi, \theta, \psi, \dot{X}_{\mathrm{b}}, \dot{Y}_{\mathrm{b}}, \dot{Z}_{\mathrm{b}}, \dot{\phi}, \dot{\theta}, \dot{\psi}) \tag{5}$$

where $(X_{\mathrm{e}}, Y_{\mathrm{e}}, Z_{\mathrm{e}})$ is the position of the center of mass in the Earth frame, (ϕ, θ, ψ) are, respectively, roll, pitch and yaw angles, and $(\dot{X}_{\mathrm{b}}, \dot{Y}_{\mathrm{b}}, \dot{Z}_{\mathrm{b}})$ are the linear velocity components described in the body frame.

The dynamical equations of motion can be described in the Earth frame as a function of the drag forces applied on the fins:

$$m\boldsymbol{a} = m\boldsymbol{g} + \boldsymbol{F}_{\mathrm{d}} \tag{6}$$

where $\boldsymbol{F}_{\mathrm{d}}$ is the drag applied on the four fins and the fuselage in the Earth frame. Defining the Direction Cosine Matrix (DCM) between the Earth frame and the body frame in the $\phi/\theta/\psi$ order, Eq. 6 can be rewritten as

$$m\boldsymbol{a} = m\boldsymbol{g} + \mathrm{DCM}^{-1}\Big(\sum_{i=1}^{4} \boldsymbol{F}_{\mathrm{di}} + \boldsymbol{F}_{\mathrm{db}}\Big) \tag{7}$$

where $\boldsymbol{g}$ is the gravitational acceleration, $\boldsymbol{a} = (\ddot{X}_{\mathrm{e}}, \ddot{Y}_{\mathrm{e}}, \ddot{Z}_{\mathrm{e}})$ is the rocket's acceleration in the Earth frame, F_{di} is the drag on the i-th fin and F_{db} is the drag on the fuselage. The force F_{db} is modeled as

$$F_{\mathrm{db}} = \frac{1}{2}\rho S_{\mathrm{b}} V_{\mathrm{air}}^2 C_{\mathrm{xb}} \tag{8}$$

where ρ is the air density at the rocket's altitude (calculated according to the 1976 COESA Atmosphere Model), S_{b} is the reference area taken as the bottom section of the rocket, and V_{air} is the airspeed. The coefficient C_{xb} is the drag coefficient for a circular plane section of a cylinder, estimated to $C_{\mathrm{xb}} = 1$ for the values of the Reynolds number in the model-scale flight conditions.

For writing the expression of the drag force F_{di} — which depends on the κ angle of the fin but also on the angle of attack α and the sideslip angle β — fin-linked angles of attack and sideslip angles are

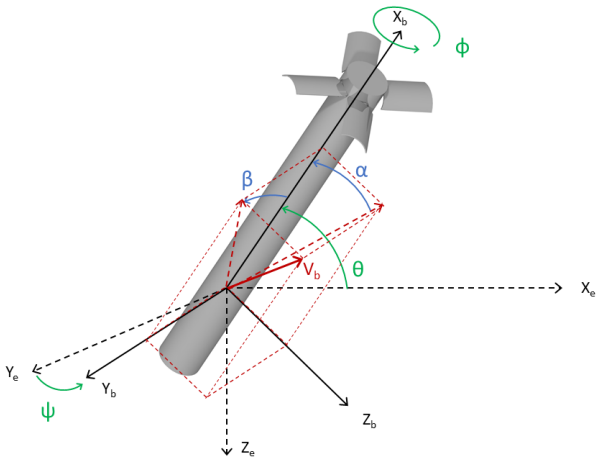

Fig. 4 Rocket orientation angles in Earth frame and angle of attack α and sideslip angle β.

defined as

$$\begin{pmatrix} \alpha_1 \\ \beta_1 \end{pmatrix} = \begin{pmatrix} \cos\pi/6 & -\sin\pi/6 \\ \sin\pi/6 & \cos\pi/6 \end{pmatrix} \begin{pmatrix} \alpha \\ \beta \end{pmatrix} \tag{9}$$

$$\begin{pmatrix} \alpha_2 \\ \beta_2 \end{pmatrix} = \begin{pmatrix} \cos\pi/6 & \sin\pi/6 \\ -\sin\pi/6 & \cos\pi/6 \end{pmatrix} \begin{pmatrix} \alpha \\ \beta \end{pmatrix} \tag{10}$$

$$\begin{pmatrix} \alpha_3 \\ \beta_3 \end{pmatrix} = \begin{pmatrix} -\cos\pi/6 & \sin\pi/6 \\ -\sin\pi/6 & -\cos\pi/6 \end{pmatrix} \begin{pmatrix} \alpha \\ \beta \end{pmatrix} \tag{11}$$

$$\begin{pmatrix} \alpha_4 \\ \beta_4 \end{pmatrix} = \begin{pmatrix} -\cos\pi/6 & -\sin\pi/6 \\ \sin\pi/6 & -\cos\pi/6 \end{pmatrix} \begin{pmatrix} \alpha \\ \beta \end{pmatrix} \tag{12}$$

where the $\pi/6$ angle is justified by Fig. 2.

The drag force F_{di} is then expressed in the fin frame as

$$F_{\mathrm{di}} = \frac{1}{2}\rho S_{\mathrm{b}} V_{\mathrm{air}}^2 C_{\mathrm{xf}} \sin\kappa_i \cos\alpha_i \cos\beta_i \tag{13}$$

Finally, as shown by Eq. 13, the κ_i angles create differences in forces that yield pitch and yaw moments that tilt the resultant drag, creating horizontal force components that translate the rocket. Similarly, the lift force applied on each fin can be expressed in the fin frame as

$$F_{\mathrm{li}} = \frac{1}{2}\rho S_{\mathrm{b}} V_{\mathrm{air}}^2 C_{\mathrm{zf}} \sin\kappa_i \cos\alpha_i \cos\beta_i \tag{14}$$

As previously mentioned, due to the orientation of the four lift forces, the resultant lift is negligible compared to the total drag. Only roll moments induced by lift forces are then considered. The point of application of those forces are taken as the center of the fins, which leads to

$$M_\phi = \sum_{i=1}^{4} \frac{1}{2}(D + L_{\mathrm{f}} \sin\kappa_i) F_{\mathrm{li}} \tag{15}$$

$$M_\theta = \frac{1}{2}\left[(D + L_\mathrm{f}\sin\kappa_1) - (D + L_\mathrm{f}\sin\kappa_2) - (D + L_\mathrm{f}\sin\kappa_3) + (D + L_\mathrm{f}\sin\kappa_4)\right]\sin\pi/6F_\mathrm{di} \tag{16}$$

and

$$M_\psi = \frac{1}{2}\left[(D + L_\mathrm{f}\sin\kappa_1) + (D + L_\mathrm{f}\sin\kappa_2) - (D + L_\mathrm{f}\sin\kappa_3) - (D + L_\mathrm{f}\sin\kappa_4)\right]\cos\pi/6F_\mathrm{di} \tag{17}$$

Simulation of the above equations of motion for our rocket configuration in free fall yields the results in Fig. 5, in which the desirable passive stability and low terminal speed are achieved.

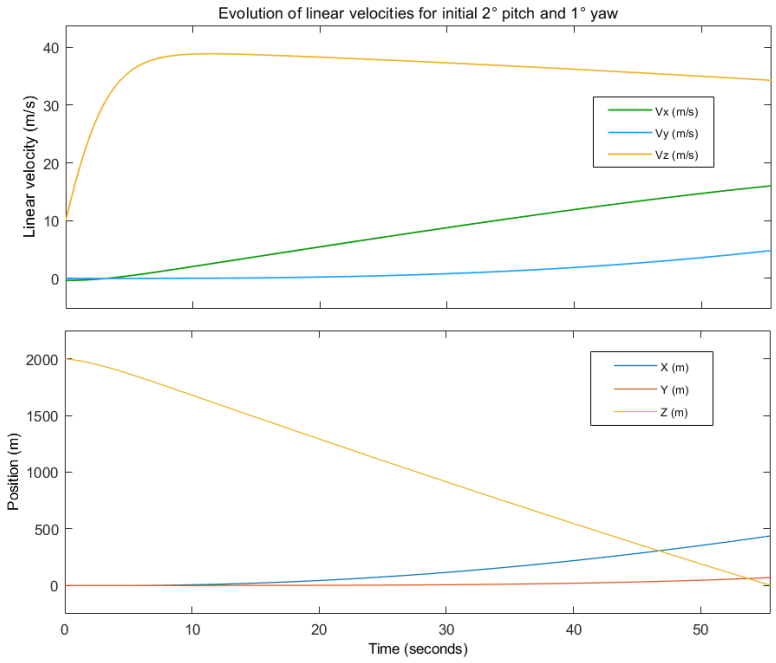

Fig. 5 Simulation of the trajectory (in m) and earth-relative speed (in $\mathrm{m\,s^{-1}}$) with fully deployed fins and initial 2° pitch and initial 1° yaw.

3 Second Phase: Thrust Vector Control Landing

The second phase brings the rocket to zero touchdown speed using only Thrust Vectoring Control (TVC). Naturally, aerodynamic actuators have low aerodynamic efficiency in the final low-speed approach. Thus, the purpose of this section is to study the existence of a feasible descent trajectory that robustly drives the rocket to a state within predefined landing bounds using TVC. Finally, this section studies the controller's performance and robustness in non-ideal scenarios.

The landing trajectory is implemented with Nonlinear Model Predictive Control (NMPC). NMPC is an optimal approach to simultaneously solving trajectory generation and control given state and actuator constraints. NMPC is directly applicable to non-linear plants and mitigates some higher-order controllability issues in linearized systems.

A significant challenge faced in this phase is the lack of a throttleable engine due to solid propellant usage. Accelerations are obtained instead by thrust direction modulation. NMPC should deflect thrust directions to achieve zero altitudes with low speed so that the landing gear can dampen the residual vertical speed and leave the rocket vertically on the ground.

3.1 Dynamics Model of the TVC Rocket

Due to the symmetry of the problem, a longitudinal three degrees-of-freedom rigid body model reduces the NMPC optimization search space. Naturally, this assumes that the preceding aerodynamic phase of the landing procedure yielded zero terminal angular motion. The actuating forces on the vehicle are then the engine thrust, the drag force, and the weight (the pressure and gravity centers are approximated to the same position in the body axes).

The Phase 2 model assumes constant gravity and flat Earth. The resulting equations of motion are

$$\dot{u} = T\cos\delta + \frac{1}{2}\rho S V^2 C_{\mathrm{xb}} - g\sin\theta - qw \tag{18}$$

$$\dot{w} = -T\sin\delta + g\cos\theta + qu \tag{19}$$

$$\dot{q} = \frac{-T\sin\delta(X_{\mathrm{CG}} - X_{\mathrm{THR}})}{I_{\mathrm{y}}} \tag{20}$$

$$\dot{\theta} = q \tag{21}$$

and

$$\begin{pmatrix} \dot{x} \\ \dot{z} \end{pmatrix} = \begin{pmatrix} \cos\theta & -\sin\theta \\ \sin\theta & \cos\theta \end{pmatrix} \begin{pmatrix} u \\ w \end{pmatrix} \tag{22}$$

where x and z denote horizontal and vertical positions of the vehicle. The state θ is the angle of the rocket in the longitudinal plane of motion. The states u, v and q represent the linear velocities in the X and Z body axes and the angular rate, respectively. The input variable δ denotes the gimbal angle with respect to the rocket (positive for a pitch-down maneuver).

Table 1 Characteristic parameters of the vehicle.

Mass [kg]	Inertia [kg m^2]	Length [m]	Surface [m^2]	Diameter [mm]	X_{CG} [m]	X_{THR} [m]
3	0.12	0.70	0.0043	74	0.17	-0.35

Finally, T denotes the thrust. After searching off-the-shelf model rocketry engines for constant and predictable burn profiles, the optimum engine chosen for this experiment provides 30 Newtons of thrust (Class E) over 5 seconds. Table 1 lists the remainder of relevant rocket physical parameters.

3.2 Controller Design

The finite-horizon optimal control input $\hat{\delta}(t_0, \boldsymbol{x}_0)$ for the state $\boldsymbol{x}_0$ at instant t_0 is

$$\hat{\delta}(t_0, \boldsymbol{x}_0) = \min_{\delta(\cdot)} \int_{t_0}^{t_0+T} J(\boldsymbol{x}(\tau), \delta(\tau))\, d\tau \tag{23}$$

constrained to the nonlinear dynamics of the system $\dot{\boldsymbol{x}} = f(\boldsymbol{x}, \delta)$, as derived before, and respecting

$$\boldsymbol{x}(t_0) = \boldsymbol{x}_0 \quad \boldsymbol{x}(T) = \boldsymbol{x}_{\mathrm{tgt}} \tag{24}$$

$$\boldsymbol{a}(t_0) \leq \psi\Big(\boldsymbol{x}(t_0), \delta(t_0)\Big) \leq \boldsymbol{b}(t_0) \tag{25}$$

and

$$\boldsymbol{c} \leq \phi\Big(\boldsymbol{x}(t), \delta(t)\Big) \leq \boldsymbol{d} \tag{26}$$

where

$$\boldsymbol{x}(t) = \begin{pmatrix} x(t) & z(t) & \theta(t) & u(t) & v(t) & \dot{\theta}(t) \end{pmatrix}^T \tag{27}$$

The vector ϕ is a trajectory constraint which is enforced over the entire time horizon while ψ is an instantaneous constraint for a specific time instant. At first, to check trajectory feasibility, a initial state is specified as $\boldsymbol{x}_0 = (0, -15, \pi/2, -5, 0, 0)$, which is a potential final instant of Phase 1. We consider a landing successful if it fulfills the inequalities in Table 2.

Table 2 Successful landing requirements.

$-20\text{ m} \leq x_{\text{tgt}} \leq 20\text{ m}$	$0\text{ m} \leq z_{\text{tgt}} \leq 0.2\text{ m}$	$85^\circ \leq \theta_{\text{tgt}} \leq 95^\circ$
$-0.4\text{ m/s} \leq u_{\text{tgt}} \leq 0.4\text{ m/s}$	$-0.1\text{ m/s} \leq w_{\text{tgt}} \leq 0.1\text{ m/s}$	$-2\text{ deg/s} \leq q_{\text{tgt}} \leq 2\text{ deg/s}$

Therefore the vector ψ contains these inequalities, as well as the initial state restrictions. The input is constrained between ± 20 degrees, which is our maximum mechanical thrust vector mount deflection. Since no state constraints are being set along the trajectory, the vector ϕ only contains this actuator angle restriction. Finally, the cost function is

$$J(\boldsymbol{x}, \delta) = \frac{1}{2}\hat{\boldsymbol{x}}^T Q \hat{\boldsymbol{x}} + \frac{1}{2}\delta^T P \delta \tag{28}$$

with $\hat{\boldsymbol{x}} = \boldsymbol{x} - \boldsymbol{x}_{\text{tgt}} = (x, z, \theta - \pi/2, u, w, q)$ and $\boldsymbol{x}_{\text{tgt}} = (0, 0, \pi/2, 0, 0, 0)$ the target state at touchdown. The weighting matrices are $Q = \text{diag}(0.5, 60, 150, 50, 70, 90)$ and $P = 1$, and were chosen by trial-and-error.

3.3 Simulation Results

The results are divided into two sections. Firstly, we numerically confirm the existence of a solution for the problem. Finally, the second experiment examines the controller's performance and solver convergence given varying initial state conditions.

3.3.1 Reference Trajectory Generation

To compute the optimal landing trajectory from the initial state $\boldsymbol{x}_0 = (0, 15, \pi/2, -5, 0, 0)$, `MATLAB` and its Model Predictive Control Toolbox are used. The sampling time is set to 100 ms since it is the commonplace model-scale servomotor command update frequency. Additionally, given the target has to be reached in 5 seconds (i.e., nominal engine burning time), the prediction horizon is set to 50. The control horizon is set to the prediction horizon as our current goal is to prove the existence of a solution, and we defer real-time feasibility studies to future work.

In Fig. 6, it can be observed the trajectory provided by the controller in the pitch plane for three distinct values of the input signal weight. Additionally, the optimal states and input for $P = 1$ are displayed during the 5 seconds that lasts the maneuver. Note that the first prediction is computed at $t = 0s$, measuring the initial state x_0, which explains why the vertical speed increases until the first optimal control action is applied at $t = 0.1s$. In Table 3, the trajectories provided are well within the bounds to determine a successful landing: little deviation angle from 90 degrees pitch and a low vertical speed that can be dampened safely by the vehicle's landing apparatus.

3.3.2 Landing from Non-Nominal Phase-Transition States

This section studies the robustness of the approach in view of distinct initial phase transition conditions. Feasibility is checked with altitude fixed to 15 m and vertical speed to 5 m s^{-1} while w, θ and q vary from their ideal states at the ignition point. Their testing ranges are $\theta \in \{90, 60, 120\}$ in deg, $w \in \{0, -1, 1\}$ in m s^{-1} and $q \in \{0, -5, 5\}$ in deg s^{-1}.

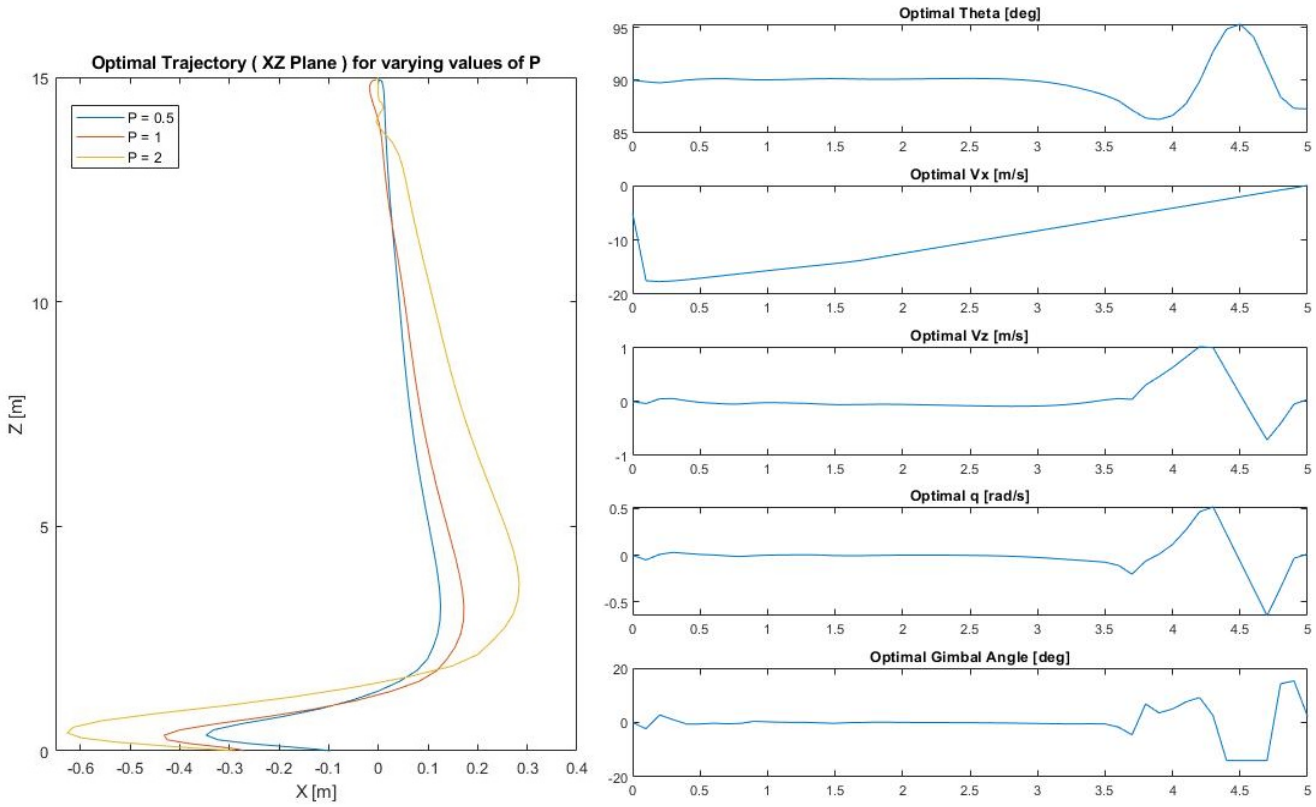

Fig. 6 Descent trajectories for P=0.5, P=1 and P=5 in the pitch plane (left) and optimal state/input signals for P=1 during the 5-second landing maneuver (right).

Table 3 Final states reached for different input signal weights P.

	x_{final} [m]	z_{final} [m]	θ_{final} [deg]	u_{final} [m/s]	w_{final} [m/s]	q_{final} [deg/s]	$J(\boldsymbol{x}, \delta)$
P=0.5	-0.096	$3.36\ 10^{-9}$	86.76	0.12	-0.086	0.80	**1.54**
P=1	-0.27	$3.36\ 10^{-9}$	87.28	0.11	0.040	0.80	**2.18**
P=2	-0.29	$3.36\ 10^{-9}$	86.71	-0.012	-0.10	0.80	**4.57**

The results in Figs. 7, 8 and 9 show the impact of drifting away from the nominal initial state x_0 when the engine is ignited. Feasible solutions exist for some of the test points that have been proposed. In tables 4, 5 and 6, it can be observed that the worst effect is induced as the vehicle presents a non-zero initial angular rate, setting the final vertical speed outside the acceptable range: stabilizing the rotating motion and fulfilling the target velocity constraints in such little time precludes controller convergence. With that said, such study provides maximum values so that the rocket can correct itself and still land safely. These limits naturally define the accuracy required in the first phase, and a second rocket design iteration is scheduled as future work based on the preliminary data shown herein.

4 Conclusion

An approach to implement autonomous landing of model-scale rockets is proposed and explored. The novel combination of Aerodynamic Passive Control for high altitudes and TVC using Model Predictive Control for low altitudes seems to properly guide the vehicle from the apogee to the ground with zero speed touchdown. NMPC transparently handles the new model-scale challenges regarding engine non-throttleability and strict time-to-touchdown requirements.

Table 4 Final states reached for varying initial pitch angle values θ.

	x_{final} [m]	z_{final} [m]	θ_{final} [deg]	u_{final} [m/s]	w_{final} [m/s]	q_{final} [deg/s]
$\theta_0 = 60°$	-8.02	$7.41\ 10^{-10}$	90.47	-0.29	0.011	1.03
$\theta_0 = 90°$	-0.27	$3.36\ 10^{-9}$	87.28	0.11	0.040	0.80
$\theta_0 = 120°$	0.41	3.76^{-9}	89.65	0.019	0.0020	-0.039

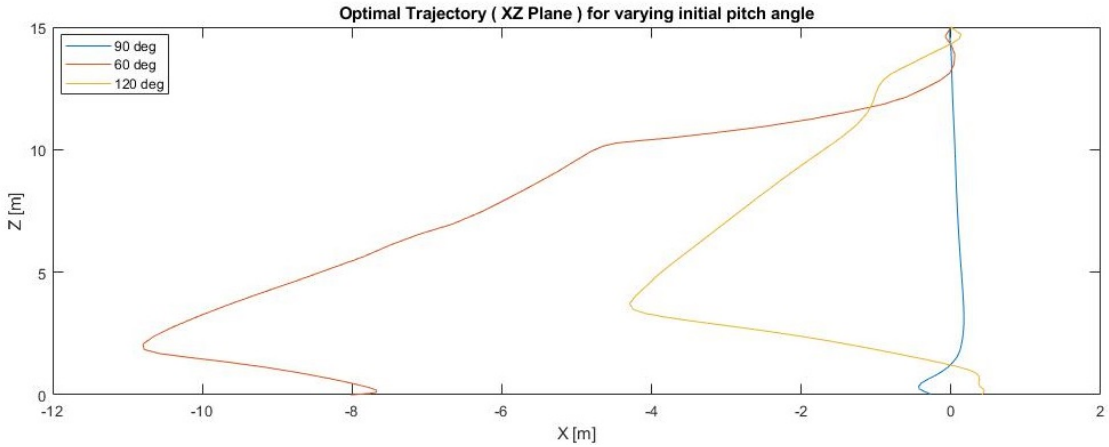

Fig. 7 Optimal descent trajectories for varying initial values of θ.

A second design iteration is scheduled as future work to accommodate the TVC initial state requirements with the resulting Aerodynamic Passive Control terminal speeds.

References

[1] Stephen A. Cook. The reusable launch vehicle technology program. In *International Space Planes and Hypersonic Systems and Technologies Conferences*. AIAA Paper 1995-6153, 1995. DOI: 10.2514/6.1995-6153.

[2] M. Gallaher, D. Coughlin, and D. Krupp. A guidance and control assessment of three vertical landing RLV. In *Guidance, Navigation, and Control Conference*. AIAA Paper 1996-3702, 1996. DOI: 10.2514/6.1996-3702.

[3] Hiroshi Yamakawa, Ken Higuchi, Tatsuya Maruyama, and Nobuyuki Kubota. Flight evaluation of GN&C system and vertical landing dynamics of reusable rocket vehicle. In *10th AIAA/NAL-NASDA-ISAS International Space Planes and Hypersonic Systems and Technologies Conference*, 2001. DOI: 10.2514/6.2001-1907.

[4] Huan Zhang, Zhihua Zhao, Gexue Ren, Pengxiang Hu, Yunfei Yang, Zhongwen Pan, and Francesco Sanfedino. Arresting-cable system for robust terminal landing of reusable rockets. *Journal of Spacecraft and Rockets*, 58(2):425–443, 2021. DOI: 10.2514/1.A34646.

[5] Marco Sagliano, Ansgar Heidecker, José Macés Hernández, Stefano Farì, Markus Schlotterer, Svenja Woicke, David Seelbinder, and Etienne Dumont. Onboard guidance for reusable rockets: Aerodynamic descent and powered landing. In *AIAA SciTech Forum*, 2021. DOI: 10.2514/6.2021-0862.

[6] Satoshi Nonaka, Koji Watanabe, Hiroyuki Ogawa, Hiroyuki Kato, and Yoshifumi Inatani. Aerodynamics of vertical landing rocket vehicle with engine thrust in landing phase. In *44th AIAA Aerospace Sciences Meeting and Exhibit*, 2006. DOI: 10.2514/6.2006-256.

[7] Yoshinori Namera, Ryoji Takaki, Akira Oyama, Kozo Fujii, and Makoto Yamamoto. Aerodynamic shape design of the vertical landing rocket vehicle. In *28th AIAA Applied Aerodynamics Conference*, 2010. DOI: 10.2514/6.2010-4367.

Table 5 Final states reached for varying initial horizontal velocity values w.

	x_{final} [m]	z_{final} [m]	θ_{final} [deg]	u_{final} [m/s]	w_{final} [m/s]	q_{final} [deg/s]
$w_0 = -1m/s$	-6.84	$6.20\ 10^{-10}$	88.18	0.48	0.010	1.69
$w_0 = 0m/s$	-0.27	$3.36\ 10^{-9}$	87.28	0.11	0.040	0.80
$w_0 = 1m/s$	6.35	5.39^{-9}	91.50	0.46	0.0039	-1.86

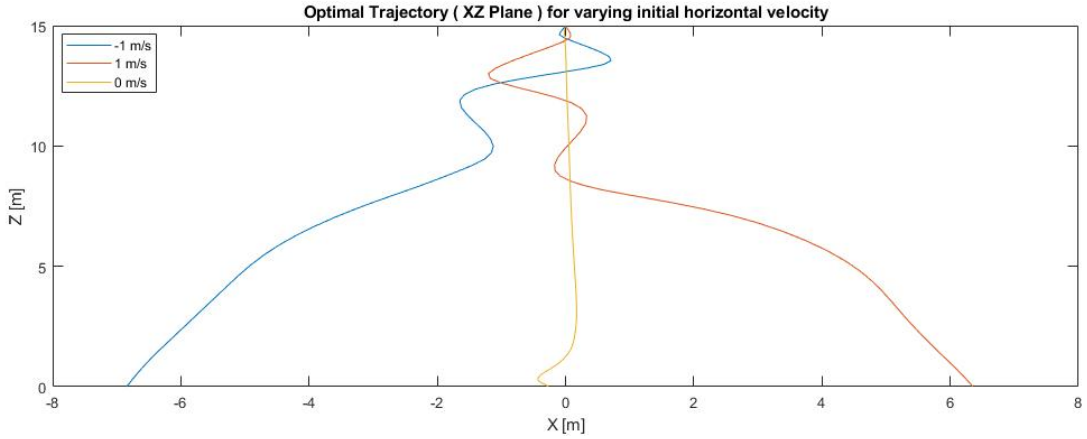

Fig. 8 Optimal descent trajectories for varying initial values of w.

Table 6 Final states reached for varying initial angular rate values q.

	x_{final} [m]	z_{final} [m]	θ_{final} [deg]	u_{final} [m/s]	w_{final} [m/s]	q_{final} [deg/s]
$q_0 = -5°/s$	-18.08	$7.89\ 10^{-15}$	93.96	-1.00	0.083	-0.41
$q_0 = 0°/s$	-0.27	$3.36\ 10^{-9}$	87.28	0.11	0.040	0.80
$q_0 = 5°/s$	19.85	$4.17\ 10^{-12}$	82.50	-0.99	-0.069	1.77

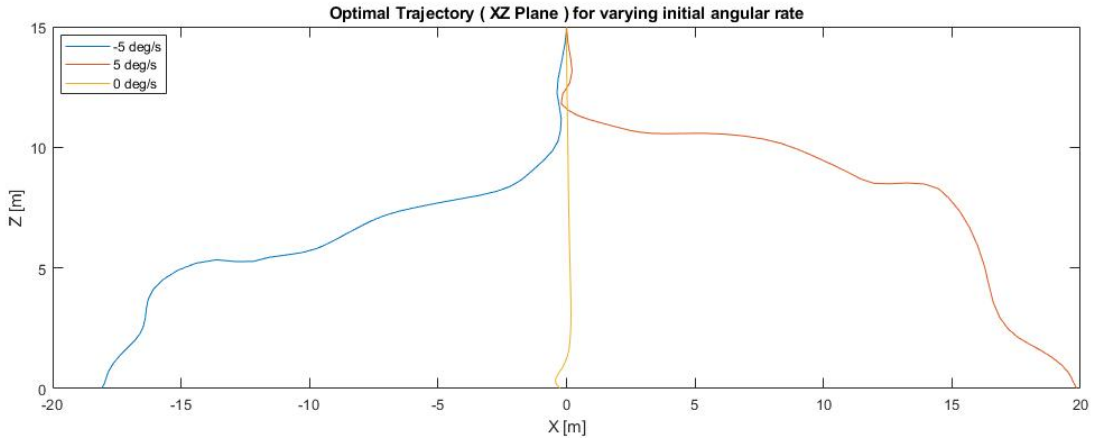

Fig. 9 Optimal descent trajectories for varying initial values of q.

[8] Zhang Bojun, Liu Zhanchao, and Liu Gang. High-precision adaptive predictive entry guidance for vertical rocket landing. *Journal of Spacecraft and Rockets*, 56(6):1735–1741, 2019. DOI: 10.2514/1.A34450.

[9] Pedro Simplício, Andrés Marcos, and Samir Bennani. Guidance of reusable launchers: Improving descent and landing performance. *Journal of Guidance, Control, and Dynamics*, 42(10):1–14, 2019. DOI: 10.2514/1.G004155.

[10] Xinfu Liu. Fuel-optimal rocket landing with aerodynamic controls. *Journal of Guidance, Control, and Dynamics*, 42(1):65–77, 2019. DOI: 10.2514/1.G003537.

[11] Jinbo Wang, Naigang Cui, and Changzhu Wei. Optimal rocket landing guidance using convex optimization and model predictive control. *Journal of Guidance, Control, and Dynamics*, 42(5):1078–1092, 2019. DOI: 10.2514/1.G003518.

[12] Michael Szmuk, Behcet Acikmese, and Andrew W. Berning. Successive convexification for fuel-optimal powered landing with aerodynamic drag and non-convex constraints. In *AIAA Guidance, Navigation, and Control Conference*, 2016. DOI: 10.2514/6.2016-0378.

[13] Lukas Spannagl, Elias Hampp, Andrea Carron, Jerome Sieber, Carlo A. Pascucci, Abu U. Zgraggen, Alexander Domahidi, and Melanie N. Zeilinger. Design, optimal guidance and control of a low-cost re-usable electric model rocket. In *IEEE/RSJ International Conference on Intelligent Robots and Systems (IROS)*, 2021. DOI: 10.1109/IROS51168.2021.9636430.